XIE, Y., WANG, S., FERNANDEZ, C., YU, C., FAN, Y. and CAO, W. 2021. A novel high-fidelity unscented particle filtering method for the accurate state of charge estimation of lithium-ion batteries. *International journal of electrochemical science* [online], 16(6), article ID 210623. Available from: https://doi.org/10.20964/2021.06.38

A novel high-fidelity unscented particle filtering method for the accurate state of charge estimation of lithium-ion batteries.

XIE, Y., WANG, S., FERNANDEZ, C., YU, C., FAN, Y. and CAO, W.

2021

© 2021 The Authors. Published by ESG (www.electrochemsci.org).

OpenAIR @RGU

This document was downloaded from https://openair.rgu.ac.uk

CC BY

Int. J. Electrochem. Sci., 16 **(2021)** Article ID: 210623, doi: 10.20964/2021.06.38

International Journal of
ELECTROCHEMICAL
SCIENCE
www.electrochemsci.org

A Novel High-Fidelity Unscented Particle Filtering Method for the Accurate State of Charge Estimation of Lithium-Ion Batteries

Yanxin Xie[1], *Shunli Wang*[1,*], *Carlos Fernandez*[2], *Chunmei Yu*[1], *Yongcun Fan*[1], *Wen Cao*[1]

[1] School of Information Engineering, Southwest University of Science and Technology, Mianyang 621010, China;
[2] School of Pharmacy and Life Sciences, Robert Gordon University, Aberdeen AB10-7GJ, UK.
[*]E-mail: 497420789@qq.com

Received: 12 February 2021 / *Accepted:* 3 April 2021 / *Published:* 30 April 2021

Power Li-ion batteries are one of the core "three powers" systems of new energy vehicles, and its accurate batteries modeling and state prediction have become the core technology of the scientific and technological progress in the industry. This paper takes the ternary Li-ion batteries as the research subject. Aiming at the mathematical expressions of different structural features, innovatively construct a second-order Thevenin equivalent circuit model with autoregressive effect. This model can characterize the internal reaction mechanism of Li-ion batteries and fit the complex electrochemical reactions inside the battery. An improved particle filter model, namely a new high-fidelity unscented particle filter method, is designed and established. By introducing a suitable suggested density function, the model can accurately calculate the mean and variance, solve the particle degradation problem, and find out the Li-ion batteries state of charge, which is suitable for complex charging and discharging conditions. By further improving the theoretical analysis and combining with experiments under different working conditions, this method studies the Li-ion batteries state of charge. The test results show that the average absolute error of the improved equivalent circuit model is reduced by 0.00457 V, and the error rate is stably kept within 1%, which has the ability to describe Li-ion batteries well. When using the high-fidelity unscented particle filter algorithm to estimate the state of charge of the lithium battery, the robustness of the system is improved, the following effect is better, and the estimation error is controlled within 1.5%, which brings good practical value to the power Li-ion batteries.

Keywords: ternary Li-ion batteries; second-order Thevenin model; autoregressive; state of charge; high-fidelity unscented particle filter algorithm

1. INTRODUCTION

In recent years, people's demand for environmentally friendly and sustainable energy development has gradually increased, and the development of new energy has increasingly become the

mainstream of development strategies [1-3]. In today's world where the green economy is booming, the automobile industry is also developing in the direction of environmental protection and energy conservation and emission reduction. Traditional cars use fossil energy as power, and the surge in car ownership has made the supply of fossil energy in short supply, affecting energy security. Developing vehicles to replace fossil energy is not only an important means of upgrading the automobile industry, but also a strategic measure of "ecological civilization". New energy vehicles are mainly researched and popularized for their advantages of energy saving, environmental protection, renewable energy, zero emission, ultra-low noise, easy using and easy maintenance. In the wave of the new energy automobile industry development, the power battery industry has maintained a momentum of sustained and rapid growth, and the enterprise capacity construction scale has expanded rapidly [4].

Compared with other batteries types, the Li-ion batteries have almost monopolized the electric vehicle power battery market due to their excellent performance, and their installed capacity is still increasing year by year [2, 5-10]. As of the end of 2019, 2.21 million new energy vehicles had been sold globally, of which China is a major new energy vehicle sales country, with sales accounting for almost half of global sales. In 2020, due to the epidemic impact, the overall market instability has increased and automobile production has shown a downward trend. However, governments around the world have stepped up their efforts and policies to support the research and development of the new energy automobile industry, and sales have maintained positive growth despite the overall automobile market recession. In 2020, the total installed capacity of batteries in the electric vehicle power industry represented by China will exceed 250 GW·h. The Li-ion batteries accounted for 97.6% of the power batteries total installed capacity, and the number of vehicles supporting it ranked first in the world. Among them, the ternary Li-ion batteries, which leads the Li-ion batteries development new round, increased by 35.3% year-on-year. It can be seen that the Li-ion batteries composition is a very obvious trend for new energy vehicle power batteries, and the occupation and loading speed are rising very fast.

In order to meet the power requirements of high-voltage and large-capacitance batteries in electric vehicles, Li-ion batteries are often combined in series and parallel. However, over-charge, over-discharge, over-heating and other phenomena often occur to the batteries charging and discharging process, which is inevitable, thus reducing its use efficiency and shortening the service batteries life. Inconsistency will be aggravated with the increase of usage times, and only relevant measures can be taken to restrain its aggravation, but this problem cannot be eliminated fundamentally. Battery Management System (BMS) was born in the field of electric vehicle development because it can detect batteries physical parameters, estimate the state of charge (SOC)/state of health (SOH)/state of power (SOP) and balance management, etc. Therefore, BMS can monitor the Li-ion batteries working state, balance and control the inconsistency, and prevent the polarization phenomenon such as ohmic polarization, concentration polarization and electrochemical polarization during the battery packs charging process. Among them, the Li-ion batteries SOC characterize the remaining batteries capacity, and accurate estimation can judge the timing of equilibrium more accurately for the BMS, and provide reference for drivers to predict the remaining mileage. The ternary Li-ion batteries are selected as the research object, estimate the power batteries SOC, and detect the SOC value.

Basic SOC estimation methods include discharge experiment method, ampere-hour (Ah) integration method and open circuit voltage method. They are the earliest studied, most mature and

classic SOC estimation methods, and they are the basis of all subsequent SOC estimation methods. There are more or less shadows in modern SOC estimation methods, and it is necessary to conduct research on basic SOC estimation methods. (1) Discharge experiment method. It uses current I certain value for continuous discharge at the rated power Q_N of the Li-ion batteries, and terminates the discharge when the voltage is lower than a preset threshold voltage. It is the simplest and most reliable estimation method, but it takes a lot of time, cannot be estimated online, and is difficult to promote in actual products; (2) Ah integral method. This method principle is to assume that the initial SOC is known, then the SOC value at any moment can be obtained by integrating the discharge current over time [11-13]. This method is easy to implement because only a current measuring device needs to obtain $I(t)$ in real time during charging and discharging to estimate the SOC value online. This method shortcomings are also obvious. One is that it is difficult to accurately obtain the initial value SOC_0, and the other is that no device can measure the time-varying $I(t)$ without errors. The former brings initial error, and the latter brings cumulative error. Therefore, the Ah integration method is not suitable for scenarios that require real-time high-precision SOC estimation; (3) Open circuit voltage method. It is estimating SOC method based on the measured voltage when the Li-ion batteries two ends are open. Its principle is that if the Li-ion batteries are left for a long time, the batteries internal electrochemical reaction will tend to be stable. At this time, there is a relatively stable mapping between the open circuit voltage and the SOC. Compared with the Ah integration method, this method does not need to care about the initial SOC value or the process of battery discharge, only the current open circuit voltage is required. However, this method relies on the voltage accurate measurement and requires higher voltage measuring instruments. At the same time, this method can only measure the batteries that has been left for a long time. Because the batteries internal electrochemical reaction is violent during the charging and discharging process, the open circuit voltage and the electromotive force are different, so there is a non-negligible estimation of the batteries SOC values in the charging and discharging state error.

It can be found in the above analysis that these three methods cannot cope with real-time estimation and cannot solve the low SOC estimation accuracy problem. In order to meet the industry's demand for high-precision real-time estimation of SOC values, modern SOC estimation methods developed based on modern time series analysis theory or modern adaptive control theory have been successively proposed.

1. Kalman filtering (KF) method. This method idea is to use the state equation to describe the Li-ion batteries of electric vehicles, take the SOC as the system state component, and use the KF theory to process the state equation to estimate the Li-ion batteries SOC [14-23]. In order to adapt to the nonlinear characteristics presented by the Li-ion batteries, the extended Kalman filter (EKF) method is applied to improve the estimation accuracy [24-34]. With the increasing requirements for SOC estimation performance in the industrial production process, estimation methods based on the unscented Kalman filter (UKF) method are also being actively explored. It fits the probability density function by sampling the system state variables, so it has good estimation accuracy [35-40]. Using the UKF algorithm to estimate SOC can significantly reduce the estimation error and further ensure the system stability. Estimating SOC based on the KF algorithm is the current research hot and mainstream idea, and many new estimation methods are continuously proposed and applied.

2. Neural network method. The SOC estimation method for Li-ion batteries developed based on artificial neural network theory has strong applicability in different application scenarios. The neural network core idea is that multiple nonlinear processing units work in parallel. By adjusting the connection weights of these processing units, a large class of nonlinear functions can be fitted. By setting the appropriate network depth and training the appropriate connection weights, a neural network for SOC estimation is constructed, and a very accurate SOC value can be estimated based on the neural network method. Estimating SOC based on neural networks and integrating other estimation theories is a current research direction. In the latest research, the RBF-BSA method is proposed to be used in the SOC hybrid estimation. The BP neural network algorithm based on the LM algorithm and the improved momentum BP neural network are all being tried to estimate the SOC value.

3. Other adaptive algorithms. Considering basic SOC estimation methods, fusing other algorithms and combining nonlinear estimation methods, a large number of SOC estimation methods have been continuously proposed. The PF algorithm idea is to randomly sample the prior probability density to obtain a batch of particles, and then these particles whose weights can be dynamically adjusted can reflect the posterior probability density [41-45]. It has a low dependence on the probability density of the Li-ion batteries state variables, which has great advantages. However, due to the large computing resources, engineering applications will be limited by the embedded system limited computing resources. Support vector machine (SVM) theory is also a better SOC estimation method. Based on the integral terminal sliding mode observer, the SOC and SOH can be jointly and robustly estimated. Many other modern SOC estimation methods are also being proposed and studied.

Considering each algorithm advantages and disadvantages, and aiming at the calculation accuracy and complexity inherent contradictions, the high-fidelity unscented Particle filtering (HF-UPF) algorithm is proposed to estimate SOC. Discovery of online state estimation theory, breakthrough the Li-ion batteries state estimation key technology, and realize battery state monitoring with high robustness and fast convergence.

2. MATHEMATICAL ANALYSIS

2.1. Equivalent circuit modeling

In the Li-ion batteries, Li^- moves back and forth between the anode and the cathode through the electrolyte, continuously leaking and embedding on the anode and cathode plates. In this process, the mutual conversion of chemical energy and electric energy is realized. When the Li-ion batteries are discharged, Li^- falls off from the positive plate, reaches the negative plate via the electrolyte, and then embeds in the negative plate. At the same time, the electrons e^- on the negative plate reach the positive plate via the load through the positive electrode conductive coating, thereby supplying energy to the load. When the Li-ion batteries are charged, the external electric field forces Li^- to fall off from the negative pole and move to the positive pole, thus realizing the storage of electric energy. The Li-ion batteries working mechanism is shown in 0.

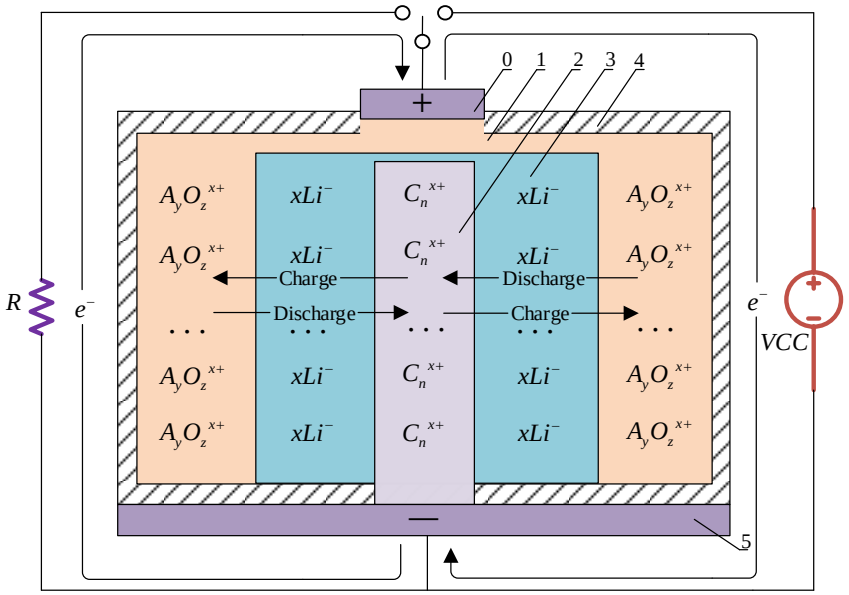

0 - Positive conductive coating 1 - Positive plate 2 - Negative plate 3 - Electrolyte 4 - Shell 5 - Negative conductive coating

Figure 1. Li-ion batteries working principle

In the 0, *R* represents the load, and VCC represents the external voltage applied to both ends of the batteries during charging. The chemical equation can clearly express the electrochemical reaction mechanism that occurs on the batteries positive and negative electrodes. The chemical reactions that occur on the positive plate (Eq. (1)), negative plate (Eq. (2)) and the entire batteries during (Eq. (3)) the charging and discharging process are as follows.

$$Li_xA_yO_z \rightleftharpoons A_yO_z + xLi + xe^- \quad (1)$$

$$nC + xLi + xe^- \rightleftharpoons Li_xC_n \quad (2)$$

$$Li_xA_yO_z + nC \rightleftharpoons Li_xC_n + A_yO_z \quad (3)$$

Where $Li_xA_yO_z$ represents a metal oxide, *A* represents a metal atom, and *O* is an oxygen atom. *C* represents a carbon atom, and graphite is usually used to form the negative electrode material. In which *x*, *y*, *z* and *n* are the corresponding atoms number. e^- refers to free electrons. When discharging, e^- starts from the negative electrode and releases electric energy through the load. When charging, e^- is forced to reverse the discharge process by the external power supply and transferred to the negative electrode to store electric energy.

Li-ion batteries have strong nonlinear dynamic characteristics due to the combination of multiple parameter coupling processes. These parameters mainly include electrochemical reaction, charge transfer and heat transfer. The complexity of the working environment and the application situation aggravated the mathematical modeling difficulty. Considering its own aging and the environment complexity and variability, the existing research aims to simulate the voltage response characteristics under different load conditions. Based on the external working characteristic data obtained in the experiment, an electrical model is constructed to describe the electrochemical reaction process inside the

Li-ion batteries. Therefore, comprehensively considered, it is innovatively proposed to apply the autoregressive (AR) model to the 2nd Thevenin (2nd-TH) equivalent circuit model. The 2nd-TH model is shown in 0.

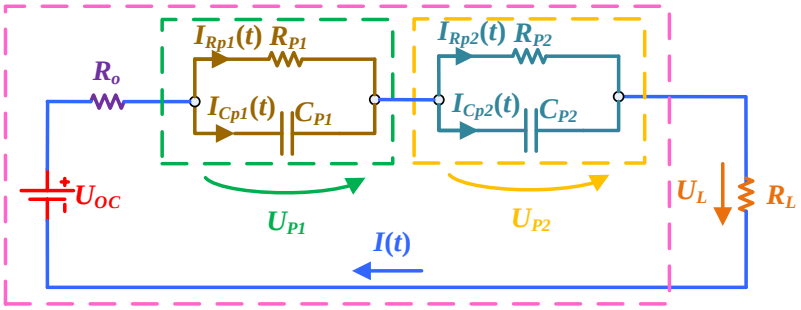

Figure 2. Li-ion batteries 2nd-TH model

In 0, U_{OC} indicates the batteries open circuit voltage, which is equal to the batteries electromotive force after the batteries are left standing for a long time. C_P and R_P are polarization capacitance and polarization resistance, respectively. $I_{Cp(t)}$ and $I_{Rp(t)}$ are the currents flowing through them respectively. The RC parallel loops can reflect the batteries polarization effect and concentration effect in the charge and discharge process. R_0 is the ohmic internal resistance. U_L is the voltage across the load, and $I(t)$ is the current flowing through the load (the value is positive when the batteries are in the charging state, and negative when the batteries are in the discharging state). According to Kirchhoff's law, the model mathematical expression is described, and the formulas are derived as follows.

$$U_L = U_{OC} - IR_0 - U_{P1} - U_{P2} \tag{4}$$

$$I = \frac{U_{P1}}{R_{P1}} + C_{P1}\frac{dU_{P1}}{dt} = \frac{U_{P2}}{R_{P2}} + C_{P2}\frac{dU_{P2}}{dt} \tag{5}$$

The AR model is a time processing method, which predicts the variable x value at time k by calculating the value of the variable x_i (i = 0,1,...,k-1) corresponding to the time t_0 - t_{k-1}. This paper chooses the second-order autoregressive (2nd-AR) model, that is, the second-order autocorrelation coefficient is tailed, and the partial autocorrelation coefficient is second-order truncated. The linear regression of the AR model is shown in Eq. (6).

$$y(k) = \varphi^T(k)\vartheta(k-1) + e(k) \tag{6}$$

Where $y(k)$ is the system output. $\varphi^T(k)$ and $\vartheta(k\text{-}1)$ are the input vector and coefficient vector respectively. $e(k)$ is the error between measurement and estimation, and it is also zero-mean Gaussian white noise. Transform the equation to obtain the system output another Eq. (7).

$$y(k) = -a_1 y(k-1) - a_2 y(k-2) + b_0 x(k) + b_1 x(k-1) + b_2 x(k-2) + e(k) \tag{7}$$

In which $x(k)$ is the system input, a_i (i = 1,2) and b_j (j = 0,1,2) are variable coefficients. The vector corresponding to $\varphi^T(k)$ and $\vartheta(k\text{-}1)$ is shown in Eq. (8).

$$\begin{cases} \varphi(k) = \left[-y(k-1); -y(k-2); x(k); x(k-1); x(k-2)\right]^T \\ \vartheta(k) = \left[a_1; a_2; b_0; b_1; b_2\right] \end{cases} \tag{8}$$

According to the Laplace transform, the Li-ion batteries impedance transfer function in the *s* domain is obtained from the Eq. (7), as shown in Eq. (9).

$$G(s)=\frac{U_L(s)-U_{OC}(s)}{I(s)}=R_0+\frac{R_{P1}}{1+sR_{P1}C_{P1}}+\frac{R_{P2}}{1+sR_{P2}C_{P2}} \tag{9}$$

The formula is transformed into Eq. (10).

$$G(s)=\frac{c_2s^2+\frac{c_3}{c_1}s+\frac{c_4}{c_1}}{s^2+\frac{c_5}{c_1}s+\frac{1}{c_1}} \tag{10}$$

The parameter c_n (n = 1,2,...,5) is shown in Eq. (11).

$$\begin{cases} c_1=R_{P1}C_{P1}R_{P2}C_{P2} \\ c_2=R_0 \\ c_3=R_0R_{P1}C_{P1}+R_0R_{P2}C_{P2}+R_{P1}R_{P2}C_{P2}+R_{P1}C_{P1}R_{P2} \\ c_4=R_0+R_{P1}+R_{P2} \\ c_5=R_{P1}C_{P1}+R_{P2}C_{P2} \end{cases} \tag{11}$$

Replace s in Eq. (10) with $\frac{1-z^{-1}}{T_sz^{-1}}$ and perform Euler transformation to obtain Eq. (12). T_s is the sampling time.

$$G(z)=\frac{b_2z^{-2}+b_1z^{-1}+b_0}{-a_2z^{-2}-a_1z^{-1}+1} \tag{12}$$

Combining Eq. (10) and Eq. (12), then the parameters of the coefficient vector $\vartheta(k)$ are as follows.

$$\begin{cases} a_1=2-\frac{c_5}{c_1}T_s \\ a_2=\frac{c_5}{c_1}T_s-\frac{1}{c_1}T_s^2-1 \\ b_0=c_2 \\ b_1=\frac{c_3}{c_1}T_s-2c_2 \\ b_2=\frac{c_4}{c_1}T_s^2-\frac{c_3}{c_1}T_s+c_2 \end{cases} \tag{13}$$

2.2. Parameter identification

Least Squares (RLS) is to select the minimum sum of squared errors for function fitting. In other words, facing a set of unknown parameters, the sum of squares of the difference between these parameters theoretical values and observed values is minimized. The RLS formulas are derived as follows.

(1) Define $\varepsilon(k)$ as the estimated error between the estimated response and the actual system feedback $y(k)$, as shown in Eq. (14).

$$\varepsilon(k)=y(k)-\varphi^T(k)\cdot\vartheta(k-1) \tag{14}$$

(2) Where $\vartheta(k\text{-}1)$ is the parameter estimated value of the at k-1.

$$\vartheta(i)=[\vartheta(i),\vartheta(i-1),\cdots,\vartheta(i-M+1)] \tag{15}$$

(3) $\varphi^T(k)$ is the branch weight vector at time k.

$$\varphi(k)=[\varphi_0(k),\varphi_1(k),\cdots,\varphi_{M-1}(k)] \tag{16}$$

(4) The gain $K(k)$ calculated by the least square method is shown in Eq. (17).

$$K(k)=P(k-1)-\varphi(k)[\lambda\cdot I+\varphi^T(k)\cdot P(k-1)\varphi(k)]^{-1} \tag{17}$$

(5) The least square method error covariance $P(k)$ is shown in Eq. (18).

$$\begin{aligned}P(k)&=\lambda^{-1}P(k-1)-\lambda^{-1}(k)K(k)\vartheta^T(k)P(k-1)\\&=[I-K(k)\cdot\varphi^T(k)]\cdot P(k-1)/\lambda\end{aligned} \tag{18}$$

(6) Calculate the prediction error and update the model parameters as shown in Eq. (19).

$$\vartheta(k)=\vartheta(k-1)+K(k)\varepsilon(k) \tag{19}$$

Thus, the time domain differential equation between the open circuit voltage and the terminal voltage is obtained.

$$\begin{aligned}U_L(k)-U_{OC}(k)=&-a_1\left(U_L(k-1)-U_{OC}(k-1)\right)\\&-a_2\left(U_L(k-2)-U_{OC}(k-2)\right)\\&+b_0I(k)+b_1I(k-1)+b_2I(k-2)\end{aligned} \tag{20}$$

From Eq. (11) and Eq. (13), the relationship expressions between the parameters of the second-order Thevenin circuit and the parameters in $\vartheta(k)$ are obtained.

$$\begin{cases}R_{P1}C_{P1}R_{P2}C_{P2}=\dfrac{T_s^{\,2}}{1-a_1-a_2}\\R_0=b_0\\R_0R_{P1}C_{P1}+R_0R_{P2}C_{P2}+R_{P1}R_{P2}C_{P2}+R_{P1}C_{P1}R_{P2}=\dfrac{2b_0-b_1}{1-a_1-a_2}T_s\\R_0+R_{P1}+R_{P2}=\dfrac{b_1+b_2}{1-a_1-a_2}\\R_{P1}C_{P1}+R_{P2}C_{P2}=\dfrac{2-a_1}{1-a_1-a_2}\end{cases} \tag{21}$$

Based on the analysis of the equivalent circuit model, the 2nd-TH model electrochemical behavior is represented by Eq. (22).

$$\begin{cases}\dot{U}_{P1}=-U_{P1}/\left(R_{P1}\times C_{P1}\right)+I/C_{P1}\\\dot{U}_{P2}=-U_{P2}/\left(R_{P2}\times C_{P2}\right)+I/C_{P2}\end{cases} \tag{22}$$

In order to study the algorithm without losing generality, suppose the nonlinear system to be processed is as Eq. (23).

$$\begin{cases}x_{k+1}=f(x_k,u_k)+w_k\\z_k=h(x_k,u_k)+v_k\end{cases} \tag{23}$$

In Eq. (23), k is the time, $x_k\in\mathbb{R}^n$ is the state space variable, and $z_k\in\mathbb{R}^m$ is the observation space variable. The zero-mean Gaussian white noise w_k and v_k are state transition noise and observation noise, respectively. w_k and v_k are independent of each other, and the w_k and v_k variances are Q_k and R_k, respectively. $f(\cdot)$ is the nonlinear state transition function, and $h(\cdot)$ is the nonlinear measurement function. u_k is the system input at time k. According to the zero state response and zero input response, the equivalent circuit model state space equation is obtained.

$$\begin{bmatrix}U_{P1,k}\\U_{P2,k}\\SOC_k\end{bmatrix}=\begin{bmatrix}e^{-T_s/\tau_1}&0&0\\0&e^{-T_s/\tau_2}&0\\0&0&1\end{bmatrix}\times\begin{bmatrix}U_{P1,k-1}\\U_{P2,k-1}\\SOC_{k-1}\end{bmatrix}+\begin{bmatrix}R_{P1}\left(1-e^{-T_s/\tau_1}\right)\\R_{P2}\left(1-e^{-T_s/\tau_2}\right)\\-\eta Cn\end{bmatrix}I(k-1)+w(k-1) \tag{24}$$

$$U_{L,k} = U_{OC,k}\left(SOC_k\right) - I_k R_0 + \begin{bmatrix} -1 \\ -1 \\ 0 \end{bmatrix}^T \begin{bmatrix} U_{P1,k} \\ U_{P2,k} \\ SOC_k \end{bmatrix} + v_k \tag{25}$$

In Eq. (24), $\tau_1 = R_{P1}C_{P1}$ and $\tau_2 = R_{P2}C_{P2}$. η represents the Li-ion batteries Coulomb coefficient, and *Cn* represents the Li-ion batteries actual capacity. According to the 2nd autoregressive Thevenin (2nd-ARTH) model analysis and the mathematical description equations establishment, as well as the description of the RLS basic principles and the specific formulas derivation. Substitute the above equations into MATLAB/Simulink for programming to realize the 2nd-ARTH model parameters identification.

2.3. Improved particle filter algorithm

2.3.1. Extended particle filter algorithm

The EKF algorithm is a local linearization method realized by the first-order Taylor expansion, which makes the system a Gaussian distribution model. According to the nonlinear system state and observation equation shown in Eq.(23). At each moment, the functions $f(x_k,u_k)$ and $h(x_k,u_k)$ are expanded by Taylor series and the higher-order terms influence on the function is ignored, and two linearization processes are completed to obtain Eq. (26) and Eq. (27).

$$\begin{cases} f(x_k,u_k) \approx f(\hat{x}_k,u_k) + \left.\dfrac{\partial f(x_k,u_k)}{\partial x_k}\right|_{x_k=\hat{x}_k} (x_k - \hat{x}_k) \\ h(x_k,u_k) \approx h(\hat{x}_k,u_k) + \left.\dfrac{\partial h(x_k,u_k)}{\partial x_k}\right|_{x_k=\hat{x}_k} (x_k - \hat{x}_k) \end{cases} \tag{26}$$

$$\begin{cases} \hat{F}_k = \left.\dfrac{\partial f(x_k,u_k)}{\partial x_k}\right|_{x_k=\hat{x}_k} \\ \hat{H}_k = \left.\dfrac{\partial h(x_k,u_k)}{\partial x_k}\right|_{x_k=\hat{x}_k} \end{cases} \tag{27}$$

According to Eq. (23), Eq. (26) and Eq. (27), the nonlinear system is transformed into a linear system, and the transformed linear system is only related to state variables. As shown in Eq. (28).

$$\begin{cases} x_{k+1} \approx \hat{F}_k x_k + \left[f(\hat{x}_k,u_k) - \hat{F}_k x_k \right] + w_k \\ z_k \approx \hat{H}_k x_k + \left[h(\hat{x}_k,u_k) - \hat{H}_k x_k \right] + v_k \end{cases} \tag{28}$$

In Eq. (28), it is noted that functions $f(\hat{x}_k,u_k) - \hat{F}_k x_k$ and $h(\hat{x}_k,u_k) - \hat{H}_k x_k$ are not the x_k functions. According to Eq. (28), the linear system is brought into the classical KF algorithm.

In the sampling stage, sampling is achieved through the mean and variance of each particle obtained by EKF. The resampling method is carried out by polynomial, which has the simplicity and low complexity advantages. Take a particle $u \sim U$ [0,1] from the [0,1] uniform distribution, satisfy x_k^i, and make the obtained particles into a new particle set.

$$\sum_{j=1}^{j-1} w_k(j) \le u \le \sum_{j=1}^{j} w_k(j) \tag{29}$$

The particle polynomial is resampled by the Eq. (29), and the particles weights are rechecked and screened to form a new particle library. The weights in these particle sets screened by the Eq. (29) are evenly distributed. The process at this stage is as follows:

(1) Initialization

Firstly, new particles are extracted and used as a new particle set. This part of particles makes it possible to obtain from the important density function of the system:

$$x_k(i) \sim p\left\{x_k \left| x_{k-1}(i)\right.\right\} \ (i=1,\ 2,\ \ldots,\ N) \tag{30}$$

The initial conditions of the filter equation state X_0 and the covariance P_0.

$$X_0 = E(X_0) \tag{31}$$

$$P_0 = E\left[\left(X_0 - \bar{X}_0\right)\left(X_0 - \bar{X}_0\right)^T\right] \tag{32}$$

(2) Update

Update the particle set and use the EKF algorithm to update the mean and variance of each independent particle in the sample. The calculation process is as follows.

i. State prior estimate.

$$\bar{X}^i_{k,k+1} = f\left(X^i_{k-1}, u^i_{k-1}\right) \tag{33}$$

ii. A priori estimate of the error covariance.

$$P^i_{k,k+1} = F^i_{k,k+1} P^i_{k-1} \left(F^i_{k,k+1}\right)^T + Q_{k-1} \tag{34}$$

iii. Kalman gain matrix.

$$K_k = P^i_{k,k+1}\left(H^i_k\right)^T \left[H^i_k P^i_{k,k-1}\left(H^i_k\right)^T + R_k\right]^{-1} \tag{35}$$

iv. State posterior estimate.

$$\bar{X}^i_k = \bar{X}^i_{k,k-1} + K_k\left[Z_k - h\left(\bar{X}^i_{k-1}, u^i_k\right)\right] \tag{36}$$

v. The posterior estimate of the error covariance.

$$P^i_k = P^i_{k,k-1} - K_k H^i_k P^i_{k,k-1} \tag{37}$$

Get the sample mean $\bar{X}^i_k$ and covariance P^i_k. Where F^i_k is the Jacobian matrix of the model states transition equation, H^i_k is the observation matrix, and K_k is the Kalman gain. Use the particle set updated by the algorithm to update the state of the i-th particle as follows.

$$\hat{X}^i_k \sim q\left(\bar{X}^i_k \mid X^i_{0:k-1}, Z_{1:k}\right) = N\left(\bar{X}^i_k, P^i_k\right) \tag{38}$$

$$\hat{X}^i_{0:k} = \left(X^i_{0:k-1}, \bar{X}^i_k\right) \tag{39}$$

$$\hat{P}^i_{0:k} = \left(P^i_{0:k-1}, P^i_k\right) \tag{40}$$

Therefore, according to Eq. (38), Eq. (39) and Eq. (40), the each particle weight w^i_k is calculated.

$$q\left(\chi_k \mid X^i_{0:k}, y\right) = p\left(x_k \mid \chi^i_{k-1}\right) \tag{41}$$

$$w^i_k = w^i_{k-1} \frac{p\left(Z_k \mid \bar{X}^i_k\right) p\left(\bar{X}^i_k \mid X^i_{k-1}\right)}{q\left(\hat{X}^i_k \mid X^i_{0:k-1}, Z_{1-k}\right)} \tag{42}$$

(3) Normalized weight

$$w_k^i = w_k^i \Big/ \sum_{i=0}^{N} w_k^i \tag{43}$$

(4) State estimation

$$\bar{x}_k = \sum_{i=1}^{N} w_k^i \chi_x^i \tag{44}$$

2.3.2. High-fidelity unscented particle filter algorithm

Utilize UKF to improve the PF algorithm and use the unscented transformation algorithm. Compared with the first-order Taylor expansion of the EKF algorithm, this method can theoretically calculate the posterior variance accuracy to the third-order and has higher accuracy. It is also an effective means to calculate mean and covariance. Based on the PF algorithm estimation framework, the core calculation of HF-UPF algorithm is as follows.

(a) Initialization

Extract particles from the prior distribution $p(X_0)$ as the new particle set initial state. These particles are obtained from the system important density function.

$$X_0^i = E\left(X_0^i\right) \tag{45}$$

$$P_0^i = E\left[\left(X_0^i - \bar{X}_0^i\right)\left(X_0^i - \bar{X}_0^i\right)^T\right] \tag{46}$$

$$X_0^{i,a} = E\left(\bar{X}_0^{i,a}\right) = \left[\left(\bar{X}_0^i\right)^T \quad 0 \quad 0\right]^T \tag{47}$$

$$P_0^{i,a} = E\left[\left(X_0^{i,a} - \bar{X}_0^{i,a}\right)\left(X_0^{i,a} - \bar{X}_0^{i,a}\right)^T\right] = \begin{bmatrix} P_0^i & 0 & 0 \\ 0 & Q & 0 \\ 0 & 0 & R \end{bmatrix} \tag{48}$$

(b) Importance sampling stage

i. Unscented transformation.

The $2n + 1$ sampling points of the state variable at the current moment are calculated by distributed sampling method, where n is state space X dimension. For the nonlinear system given by Eq. (23), the UT process is performed on it. And make the mean and variance of the Sigma point set correspondingly equal to the state variable at the current moment. Suppose the mean value of X is $\bar{X}$, then the sampling point is determined by Eq. (49).

$$\begin{cases} X_0 = \bar{X}_0 \\ X_i = \bar{X}_i + \sqrt{(n_a + \lambda)P_i}, i = 1, \cdots, n \\ X_i = \bar{X}_i - \sqrt{(n_a + \lambda)P_i}, i = n+1, \cdots, 2n \end{cases} \tag{49}$$

In the above formula, X_i represents the i-th sampling point, and $\sqrt{(n_a + \lambda)P_i}$ represents the i-th column of the matrix $\sqrt{(n_a + \lambda)P}$ .Corresponding to each X_i, its weight is given by Eq. (50) when calculating the mean.

$$\begin{cases} \omega_0^m = \dfrac{\lambda}{n+\lambda} \\ \omega_0^c = \dfrac{\lambda}{n+\lambda} + 1 - \alpha^2 + \beta, i = 1, \cdots, 2n \\ \omega_i^m = \omega_0^c = \dfrac{1}{2(n+\lambda)} \\ \lambda = \alpha^2 (n+\gamma) - n \end{cases} \tag{50}$$

In Eq. (50), ω_i^m represents the weight of the i-th sampling point in calculating the mean value, and ω_i^c represents the weight of the i-th sampling point in calculating the covariance. The *n* is the dimension degree of state variable *x*. The α factor is the distribution state of the sampling points around the mean. The α controls the distance between the sampling points and the mean. The α generally takes a constant of $\alpha \in (10^{-6}, 1)$. γ is required to satisfy $\gamma + n \neq 0$. Because of $n \neq 0$, $\gamma = 0$ can generally be selected. β is a priori distribution factor. Since it has been assumed that the system given by Eq. (23) obeys Gaussian distribution, $\beta = 2$ is optimal. The λ parameter represents the zoom ratio.

ii. Sigma point set update.

Sigma point set update is the process of using the state space sampling points obtained by the UT at the previous moment to predict the sampling points at the current moment. It is also the Sigma further prediction, given by Eq. (51). Where $\bar{X}_{k|k-1}^{i,a}$ is given by Eq. (49).

$$\bar{X}_{k|k-1}^{i,a} = f\left(X_{k-1}^{i,x}, X_{k-1}^{i,v}\right) \tag{51}$$

iii. State variable *X* and covariance *P* prediction.

Multiply the Sigma points predicted values in Eq. (51) by the corresponding weight in Eq. (50) to obtain the *x* predicted value at the next moment, as shown in Eq. (52). Then the covariance is calculated from the *x* predicted value and the covariance weight, and the calculation formula is given by Eq. (53).

$$\bar{X}_{k|k-1}^{i} = \sum_{j=0}^{2n_a} \omega_j^m X_{j,k|k-1}^{i,x} \tag{52}$$

$$P_{k|k-1}^{i} = Q_k + \sum_{j=0}^{2n_a} \omega_j^c \left[X_{j,k|k-1}^{i,x} - \bar{X}_{k|k-1}^{i} \right] \left[X_{j,k|k-1}^{i,x} - \bar{X}_{k|k-1}^{i} \right]^T \tag{53}$$

iv. Observations further prediction.

The KF algorithm not only needs to predict the state and covariance at $k + 1$ from the state at time *k*, but also needs to predict the state of the observation space at time $k + 1$. Eq. (50) and Eq. (53) have predicted the state and covariance at $k + 1$. In the UKF algorithm, to predict the observation space at time $k + 1$, the observation predicted value at time $k + 1$ needs to be calculated from the state at time *k*, as shown in Eq. (54).

$$Z_{k|k-1}^{i} = h\left(X_{k|k-1}^{i,x}, X_{k-1}^{i,n}\right) \tag{54}$$

v. System observation matrix and covariance matrix prediction.

Observations obtained by nonlinear transfer based on sampling points given by Eq. (54) are averaged to obtain the predicted amount of the system observation matrix. Then calculate the variance of the observed measurement at $k + 1$ given by the predicted value, and the covariance between it and the state variable. The Eq. (55) gives the calculation method of the prediction system observations, and

the observations variance is given by the Eq. (56). Finally, the covariance between the observed quantity and the state quantity is shown in Eq. (57).

$$\bar{Z}_{k|k-1}^{i} = \sum_{j=0}^{2n_a} \omega_j^m Z_{k|k-1}^{i} \tag{55}$$

$$P_{\bar{Z}_k} = R_k + \sum_{j=0}^{2n_a} \omega_j^c \left[Z_{j,k|k-1}^{i} - Z_{k|k-1}^{i} \right] \left[Z_{j,k|k-1}^{i} - Z_{k|k-1}^{i} \right]^T \tag{56}$$

$$P_{X_k,Z_k} = \sum_{j=0}^{2n_a} \omega_j^c \left[X_{j,k|k-1}^{i} - X_{k|k-1}^{i} \right] \left[X_{j,k|k-1}^{i} - X_{k|k-1}^{i} \right]^T \tag{57}$$

vi. Status and covariance update.

Eq. (52) and Eq. (55) give the calculation method for estimating the state and observation at k + 1 from the information at time k. Next, we need the data at k + 1 for posterior estimation, that is, to modify the prior estimation to get a more accurate estimation value. Before the correction process starts, calculating the Kalman filter gain is a necessary step, as shown in Eq. (58).

$$K = P_{\bar{Z}_k} P_{X_k,Z_k} \tag{58}$$

The previous 5 steps are prepared for the status update in step vi. The covariance update is to prepare for the estimation at time k + 2. The status update is shown in Eq. (59). The covariance update is shown in Eq. (60).

$$\bar{X}_k^i = \bar{X}_{k|k-1}^i + K\left(Z_k - \bar{Z}_{k|k-1}^i\right) \tag{59}$$

$$\hat{P}_k^i = P_{k|k-1}^i - K P_{\bar{Z}_k} K^T \tag{60}$$

Where Z_k is the observation measured by the instrument at k + 1. $\bar{Z}_{k|k-1}^{i}$ is the observation obtained from the state estimation at time k. $\bar{X}_k^i$ is the posterior state estimate at k + 1, and $\bar{X}_k^i$ is the optimal state estimation at the current time.

The estimating realization process that nonlinear system state given by Eq. (23) by use UKF algorithm is given above. The optimal estimation based on the minimum variance criterion can be obtained, and the estimation accuracy is better than the EKF algorithm processed by linearization. The subsequent steps are consistent with the EPF algorithm flow.

2.3.3. Algorithmic joint estimation

When the PF algorithm is completed, the extracted particles have a great impact on the calculation accuracy, and the main impacts are as follows: 1. The imbalance caused by different particles weights; 2. if there are a large number of particles with small weight, a large amount of calculation time will be used to calculate the particles with smaller weights, which will greatly reduces the calculation efficiency and accuracy, that is, the PF algorithm will degenerate.

Although resampling can reduce particle degradation and improve calculation accuracy, it also increases the calculation amount of the algorithm, and decreases the algorithm calculation efficiency. At the same time, too many resampling times will eliminate a large number of particles, greatly reduce the particle library and seriously exhaust the particle library. Therefore, in order to ensure that the effective number of particles will not be depleted due to a large reduction in resampling, the reasonable suggested

density function can be set in the application, so that the likelihood function is basically consistent with the prior distribution, and the samples in the particle concentration are largely transferred to the area covered by the likelihood function, the threshold value guarantees the number of particles. This paper uses EKF and UKF as the suggested density functions to further optimize the algorithm. The specific algorithm flow chart is shown in 0.

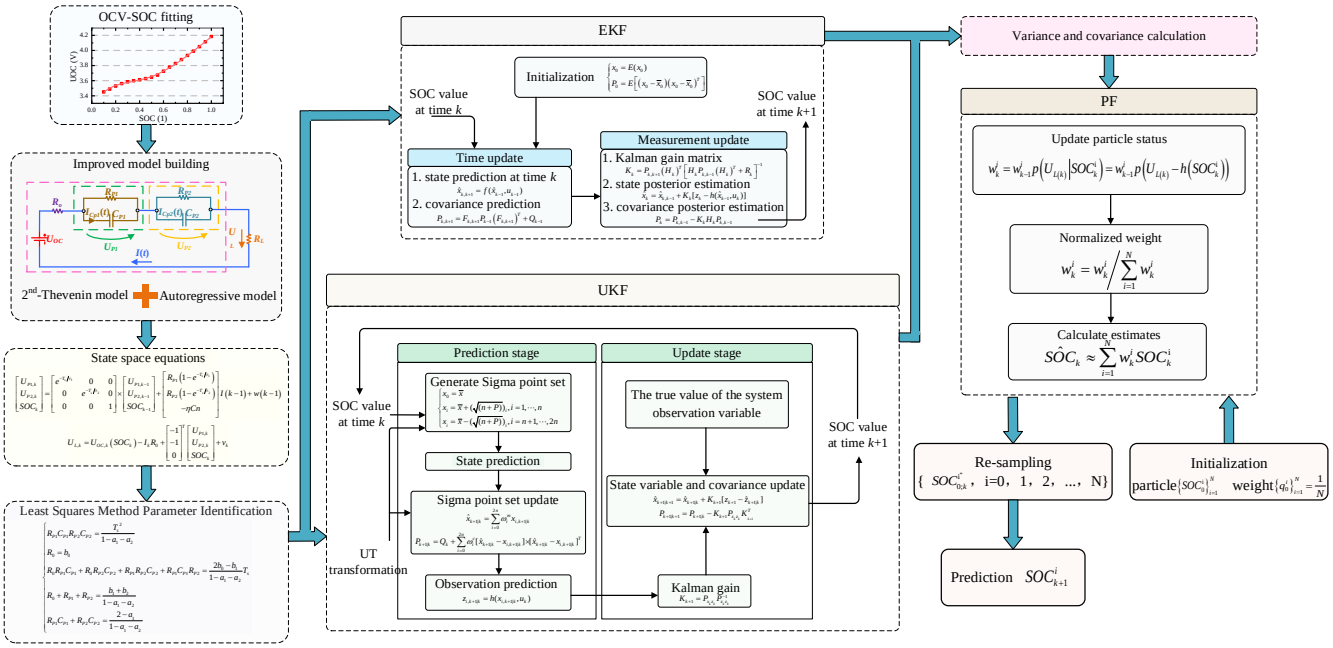

Figure 3. Joint estimation algorithm flowchart

According to the algorithm flow shown in 0, the PF algorithm uses EKF and UKF algorithms to update the mean and variance of each independent particle in the sample. Aiming at the depletion phenomenon of the particle set due to particle resampling, the parameter α is added to the resampling design to suppress the depletion phenomenon that the particle set may appear. This parameter needs to satisfy the Eq. (61).

$$w_t^i = \left(w_{t-1}^i\right)^{\alpha} \frac{p\left(z_t \mid x_t^i\right) p\left(x_t^i \mid \chi_{t-1}^i\right)}{q\left(x_t^i \mid x_{t-1}^i, z_{1:t}\right)} \tag{61}$$

Among them, the parameter α has a great significance meaning in the genetic algorithm. Its function is to control it according to the particle importance weight in the PF algorithm, which can reduce the exhaustion phenomenon in the sample. Through the above optimization method, the Li-ion batteries operating characteristics can be obtained, which has high practical value.

3. EXPERIMENTAL ANALYSIS

3.1. Test equipment and platform

In order to study the working characteristics of Li-ion batteries, it is necessary to carry out Li-ion batteries test experiments under different working conditions. To carry out experiments, it is necessary to build an experimental test platform, and the platform structure is shown in 0.

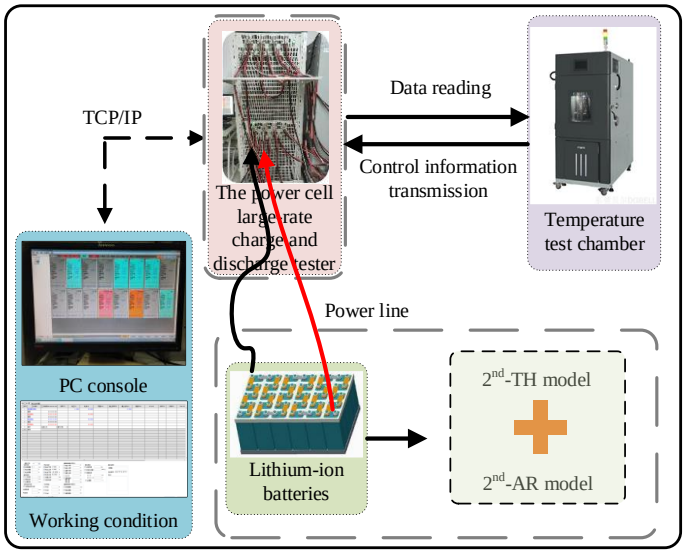

Figure 4. Li-ion batteries test platform construction

As shown in 0, the batteries test platform includes: (1) a Li-ion battery with a rated capacity of 70 Ah; (2) a battery test system (NEWARE BTS-4000) for charging and discharging Li-ion batteries. This device can detect the voltage, current and temperature of the battery, and the sampling interval is 1 s; (3) A temperature box (TT-5166-7) that provides a constant temperature environment (25 °C) for the battery. Based on the above test platform, all the Li-ion battery test experiments required in this article can be completed, and relevant experimental data can be obtained.

3.2. Online parameter identification

At the ambient temperature of 23 ℃, a Hybrid Pulse Power Characteristic (HPPC) test experiment was adopted to obtain the batteries characteristics. It is a test experiment that pulses charge and discharge the batteries under test and continuously measures the batteries terminal voltage. The batteries characteristic information is included in the terminal voltage. By processing the measured terminal voltage data, the Li-ion batteries characteristic data can be obtained. Choose SOC 1 ~ 0.1 equidistant points to carry out the experiment operation until the batteries capacity drops to 0, or when the current drops to 0.05 C, stop the experiment. In this process, each time the Li-ion batteries releases

5% of its own capacity, an HPPC cycle test is performed. 0 shows the voltage and current change curve of the Li-ion batteries terminal in the HPPC test experiment.

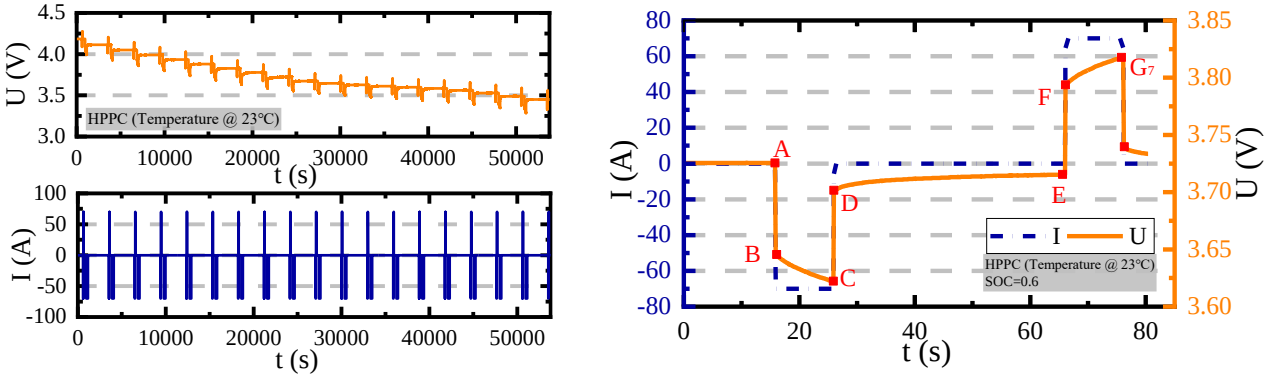

(a) HPPC voltage current curve

(b) Voltage and current amplification curve when SOC=0.6

Figure 5. Li-ion batteries terminal voltage and current changes

According to the HPPC experiment results, the AB and CD segments are the Li-ion batteries beginning and ending discharge phase. At this time, the RC network is in a zero-response state, and the reason for the sharp drop/surge in this process is mainly caused by the ohmic internal resistance. During the period corresponding to DE, the RC network is in a zero-input state. Since the circuit contains two RC networks, when the circuit structure or parameters change suddenly, the system energy is only excited by the capacitors initial energy storage in the RC network, so the terminal voltage has a gentle upward trend. Using RLS parameter identification, the model parameters under different SOC states are shown in

Table **1**.

Table 1. Model parameters under different SOC states

SOC/%	U_{OCV}/V	R_O/Ω	R_{P1}/Ω	C_{P1}/F	R_{P2}/Ω	C_{P2}/F
100	4.1846	0.001094286	3.65143E-05	23530.51643	0.000500571	29166.66667
95	4.1145	0.001121429	5.18714E-05	19278.43569	0.0006	29516.66667
90	4.0507	0.001124286	5.41714E-05	17963.34388	0.000698429	29079.56637
85	3.9908	0.001125714	5.22286E-05	18916.84902	0.000682143	27017.80105
80	3.9341	0.00113	7.12857E-05	19400.8016	0.001060429	31044.05227
75	3.8795	0.001121429	3.49571E-05	20839.80384	0.000622571	22824.69022
70	3.8275	0.001121429	4.36714E-05	14847.23585	0.000651143	23005.70426
65	3.7788	0.001125714	5.70429E-05	19844.72827	0.000826857	26340.70491

60	3.7255	0.001121429	4.17143E-05	15201.0274	0.000574429	22422.28301
55	3.6740	0.001128571	3.28143E-05	24087.07009	0.000445714	30108.97436
50	3.6467	0.001138571	0.0000294	22656.46259	0.000412	32330.09709
45	3.6272	0.001145714	0.0000231	39398.2684	0.000404571	32157.48588
40	3.6120	0.001142857	3.88571E-05	28257.35294	0.000471714	35953.96729
35	3.5990	0.001157143	3.55286E-05	33888.21874	0.000494143	35738.65279
30	3.5847	0.001152857	3.50143E-05	15439.41248	0.000482143	31608.88889
25	3.5615	0.001178571	3.30714E-05	17477.32181	0.000479429	29222.28844
20	3.5292	0.001202857	4.46714E-05	15602.8142	0.000543143	28298.26407
15	3.4895	0.001235714	5.12286E-05	10049.07975	0.000566286	22656.40767
10	3.4511	0.001287143	8.59857E-05	4989.200864	0.000741	16639.67611

To analyze and verify the feasibility and accuracy of the improved equivalent circuit model describing the Li-ion batteries used in electric vehicles, the 2nd-TH model and the 2nd-ARTH model were simulated in MATLAB/Simulink respectively. Validate the improvement model and analyze the practicability of the improvement strategy. The model accuracy is reflected according to the difference between the simulated output voltage and the actual voltage, as shown in 0.

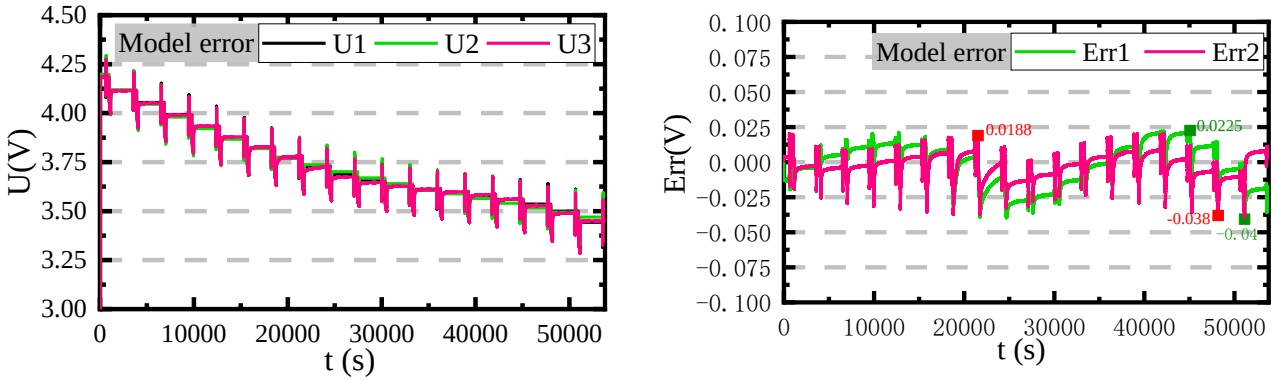

(a) Voltage comparison curve (b) Estimated error comparison curve

Figure 6. Model comparison simulation results

In 0 (a), U1 represents the Li-ion batteries actual voltage, U2 and U3 represent the simulated voltage of the 2nd-TH model and the 2nd-ARTH model, respectively. In 0 (b), Err1 represents the 2nd-TH model simulation error graph, and Err2 represents the 2nd-ARTH model simulation error graph. During the whole process, the simulation results did not show divergence, and the larger error fluctuations were caused by the pulse charging and discharging process. The two models performance parameters in equivalent Li-ion batteries are shown in

Table 2.

Table 2. Performance analysis of equivalent Li-ion batteries different models

	Maximum positive error/V	Maximum reverse error/V	Mean absolute error/V
2^{nd}-TH	0.0225	0.04	0.013925814
2^{nd}-ARTH	0.0188	0.038	0.009258075

From the data analysis in

Table 2, we can see that using AR model to improve the 2nd-TH model, the maximum voltage error is reduced by 0.002 V, the model average absolute error is reduced by about 0.00457 V, and the error rate is less than 1%. It has good stability and can more accurately characterize the batteries internal electrochemical reaction process. Therefore, it is feasible to improve the equivalent circuit model.

3.3. Algorithm comprehensive simulation

To analyze the practicability of PF in Li-ion batteries SOC estimation, the parameters are set as follows: process noise variance Q = 10, observed noise variance R = 1, particle number 50, and the filtering effect of the algorithm is analyzed, as shown in 0.

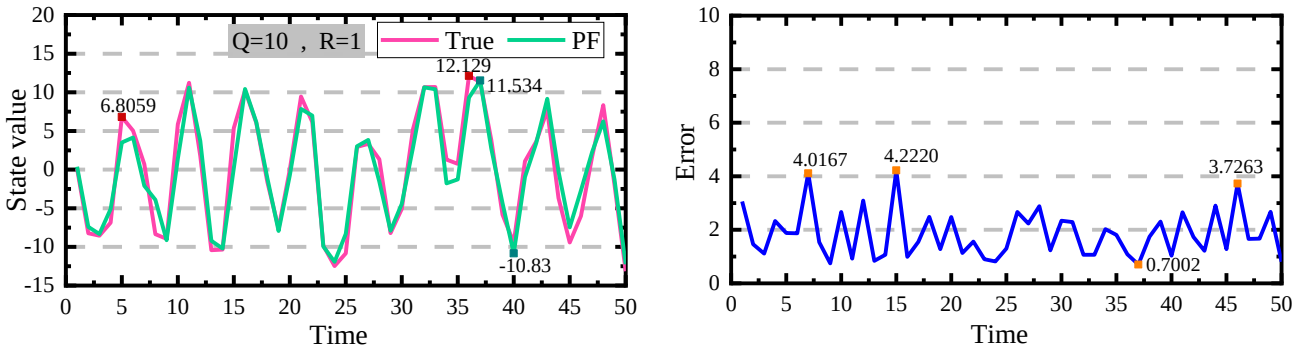

(a) Filter state estimation (b) Filter error value

Figure 7. Simulation curve based on particle filter

As shown in 0, macroscopically, the simulation based on PF has good filtering performance and basically follows the real state changes, which verifies that the PF algorithm is suitable for estimating the SOC of Li-ion batteries. Therefore, the algorithm is improved to get extended particle filter (EPF) and HF-UPF algorithms respectively. To comprehensively analyze the advantages and disadvantages of PF, EPF and HF-UPF algorithms, the initial covariance $P(0)$ = 0.75 and the time t = 50 are set. The comparison of system state, state deviation and algorithm real-time performance is shown in 0. The

system state reflects the ability of the system to follow the real state. By analyzing the difference between the system state and the real state, the state deviation diagram in 0 (b) is obtained.

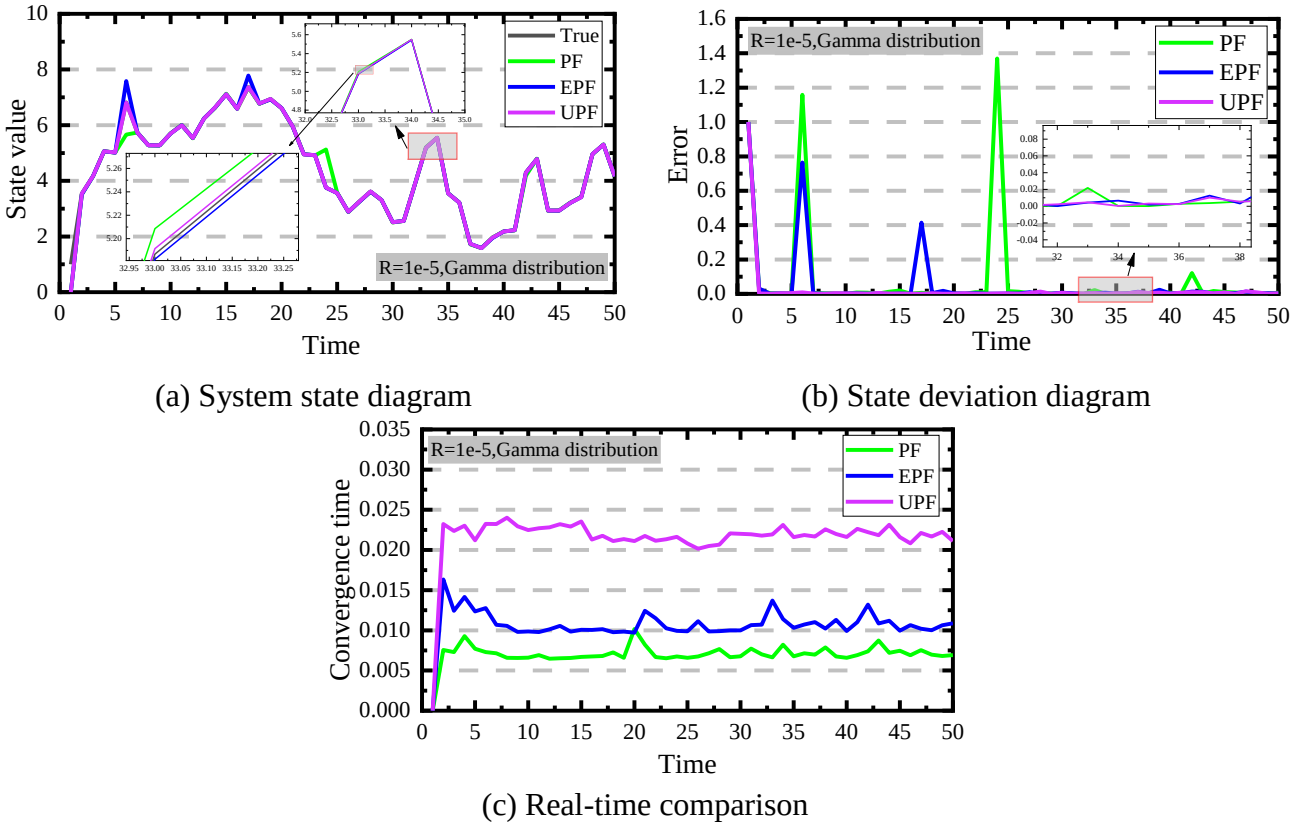

(a) System state diagram (b) State deviation diagram

(c) Real-time comparison

Figure 8. Comprehensive comparison of algorithms

According to 0, the three algorithms all follow the system state changes well. Compared with PF and EPF, the HF-UPF algorithm is closer to the real state. However, as the complexity of the algorithm increases, its consumption time also increases relatively, and its real-time performance is lower. On the other hand, it is also verified that HF-UPF algorithm is suitable for Li-ion batteries SOC estimation.

3.4. Complex condition experiment

It can be seen from Tab. 1 that the open circuit voltage, ohmic internal resistance, polarization internal resistance and polarization capacitance corresponding to the collected SOC of Li-ion batteries under different values are not regular with SOC values, and there is a one-to-one functional relationship between SOC and parameters. Through the obtained parameter values, these parameters are applied to process recurrence equation and observation noise equation, which can truly simulate the change of current and predict and estimate SOC. The test and analysis are carried out under constant current discharge conditions and Beijing bus dynamic stress test (BBDST) conditions respectively, and the SOC estimation and error tracking curves of the Li-ion batteries are shown in 0 and Fig.10.

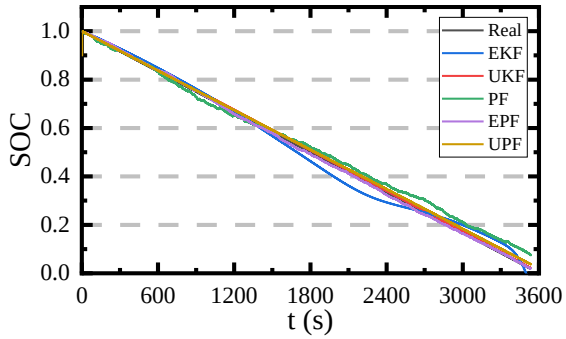

(a) SOC estimation under constant current conditions

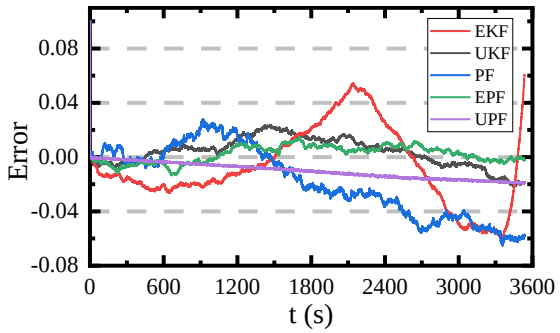

(b) Error tracking curve under constant current conditions

Figure 9. SOC estimation and error tracking curve

The core part of the improved strategy lies in particle resampling. Through particles continuous selection and training, a particle library that meets the threshold is obtained. Through the simulation image analysis in Fig.9, it is concluded that from a macro perspective, the HF-UPF algorithm has a good filtering effect on tracking the Li-ion batteries SOC. The analysis diagram is 0 (a)(b). Under the constant current discharge condition, the algorithm estimation converges rapidly in the initial stage, but as time goes by, the improvement strategy has an obvious effect in the application, which is basically stable within 2%. Comparing several current traditional SOC estimation methods, it can be seen that the improved estimation strategy is more suitable for accurate charge estimation of Li-ion batteries, and it also characterizes the superiority of the improved algorithm [46]. Therefore, the optimization algorithms are embedded in more complex working conditions for testing, and the generalization of the algorithm is analyzed. Obtain the SOC estimation under BBDST conditions, as shown in Figure 10.

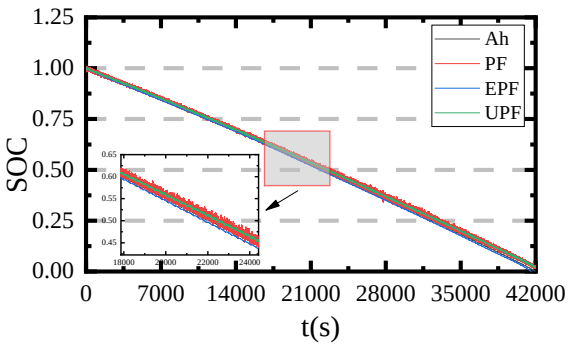

(a) SOC estimation under BBDST conditions

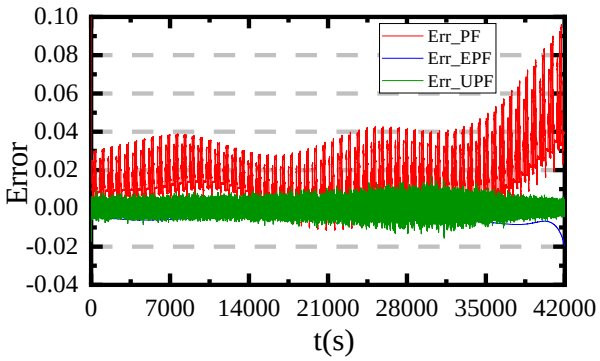

(b) Error tracking curve under BBDST conditions

Figure 10. SOC estimation and error tracking curve

In 0 (a)(b), the EPF algorithm error is within 2% under BBDST condition. The HF-UPF algorithm tracking error is basically controlled within 1.5%, the estimation accuracy is high, and the

convergence speed is fast. It can effectively improve the influence of the charge and discharge rate, temperature and life cycle on the SOC, and has reliable adaptability. According to the state-of-charge estimation method proposed in [42], the UKF algorithm combined with PF is used, and the estimation error is about 1%, but the high-fidelity battery that prevents overcharge and overdischarge is not considered. The particle arrangement rule of the process is relatively common, and the comparison is made only by the size of the weight and the threshold. However, the HF-UPF charge tracking error has been in a jitter state, and the algorithm itself is more sensitive to the noise influence, and its anti-interference ability is relatively weaker than the EPF algorithm. However, the EPF algorithm error is increasing throughout the process and cannot predict the error trend at the next moment.

4. CONCLUSIONS

In order to verify the effectiveness of the HF-UPF algorithm proposed in this paper to estimate the Li-ion batteries SOC. Through the constructed 2nd-ARTH model parameter identification of Li-ion batteries, the identification result shows that the model accuracy is over 99%. Reflects the batteries dynamic response effect and can meet the accuracy requirements under actual application conditions. Import the identified experimental result data into the SOC estimation algorithm. Compared with the PF and EPF algorithms, it is concluded that the HF-UPF algorithm has a good tracking effect and automatic convergence ability, which effectively avoids the error accumulation effect. The algorithm converges to the true value within a limited sampling period, and basically solves the Ah integral large deviation due to measurement interference or inaccurate initial value. The estimation accuracy can reach 98.5%. In fact, the PF algorithm is essentially not restricted by system factors, but the EKF and UKF algorithms application in the improvement strategy all makes Gaussian assumptions on the system, resulting in the optimization algorithm also being restricted by the Gaussian model. Need further research in practical applications.

ACKNOWLEDGMENTS
The work is supported by the National Natural Science Foundation of China (No. 61801407), Sichuan science and technology program (No. 2019YFG0427), China Scholarship Council (No. 201908515099), and Fund of Robot Technology Used for Special Environment Key Laboratory of Sichuan Province (No. 18kftk03).

References

1. J. G. Zhu, M. Knapp, MSD. Darma, Q. H. Fang, X. Y. Wang, H. F. Dai, *Appl. Energy*, 248 (2019) 149.
2. K. Yoo, J. Kim, *J. Power Sources*, 433 (2019).
3. T. Mesbahi, N. Rizoug, P. Bartholomeus, R. Sadoun, F. Khenfri, P. Le Moigne, *IEEE Trans. Ind. Electron.*, 65 (2018) 1298.
4. P. Shen, M. G. Ouyang, L. G. Lu, J. Q. Li, X. N. Feng, *IEEE Trans. Veh. Technol.*, 67 (2018) 92.
5. S. B. Xie, X.S. Hu, S. W. Qi, X. L. Tang, K. Lang, Z. K. Xin, *Energy*, 173 (2019) 667.
6. J. L. Xie, Y. Y. Xie, C. Yuan, *Int. J. Heat Mass Transfer*, 129 (2019) 1184.
7. B. Xiao, Y. G. Liu, and B. Xiao, *IEEE Access*, 7 (2019) 54192.
8. N. X. Yang, Y. H. Fu, H. Y. Yue, *Electrochim. Acta*, 311 (2019) 8.
9. Z. Yang, D. Patil, and B. Fahimi, *IEEE Trans. Veh. Technol.*, 68 (2019) 170.

10. J. S. Yu, W. Q. Tang, D. Y. Tang, J. Q. Wan, J. J. Liu, *J. Ambient Intell. Hum. Comput.*, 10 (2019) 923.
11. W. Xu, J. L. Xu, B. L. Liu, J. J. Liu, X. F. Yan, *Energy Sci. Eng.*, 8 (2020) 2784.
12. Y. D. Xu, M. H. Hu, A. J. Zhou, Y. X. Li, S. X. Li, *Appl. Math. Modell.*, 77 (2020) 1255.
13. W. Xu, J. L. Xu, X. F. Yan, *J. Power Electron.*, 20 (2020) 292.
14. S. L. Wang, C. Fernandez, C. Y. Zou, C. M. Yu, L. Chen, L. Zhang, *Energy*, 171 (2019) 444.
15. S. L. Wang, C. Fernandez, Z. W. Xie, X. X. Li, C. Y. Lou, Q. Li, *Energy Sci. Eng.*, 7 (2019) 3038.
16. S. L. Wang, C. Fernandez, W. Cao, C. Y. Zou, C. M. Yu, X. X. Li, *J. Power Sources*, 428 (2019) 67.
17. J. Su, M. Lin, S. L. Wang, J. Li, J. Coffie-Ken, F. Xie, *Meas. Control*, 52 (2019) 193.
18. S. L. Wang, C. M. Yu, C. Fernandez, M. J. Chen, G. L. Li, X. H. Liu, *J. Power Electron.*, 18 (2018) 1127.
19. C. F. Yang, X. Y. Wang, Q. H. Fang, H. F. Dai, Y. Q. Cao, X. Z. Wei, *J. Storage Mater.*, 29 (2020).
20. M. Jiao, D. Q. Wang, J. L. Qiu, *J. Power Sources*, 459 (2020).
21. F. Guo, G. D. Hu, P. K. Zhou, J. Y. Hu, Y. H. Sai, *Int. J. Energy Res.*, 44 (2020) 7357.
22. Q. T. Wang, W. Qi, *J. Power Electron.*, 20 (2020) 614.
23. Y. J. Wang, Z. H. Chen, *Appl. Energy*, 260 (2020).
24. Z. Y. Song, J Hou, X. F. Li, *Energy*, 193 (2020) 66.
25. L. J. Song, T. Y. Liang, L. G. Lu, M. G. Ouyang, *Int. J. Electr. Power Energy Syst.*, 115 (2020).
26. X. Lai, S. Y. Wang, L. He, L. Zhou, Y. J. Zheng, *J. Storage Mater.*, 27 (2020).
27. A. J. Smiley, W. K. Harrison, G. L. Plett, *J. Storage Mater.*, 27 (2020).
28. S. Li, K. Li, E. Xiao, J. H. Zhang, M. Zheng, *J. Power Sources*, 448 (2020).
29. X. L. Yang, Y. J. Chen, B. Li, D. Luo, *Energy*, 191 (2020).
30. S. L. Wang, *J. Cleaner Prod.*, 198 (2018) 1090.
31. S. L. Wang, C. Fernandez, L. P. Shang, Z. F. Li, H. F. Yuan, *Trans. Inst. Meas. Control*, 40 (2018) 1892.
32. S. L. Wang, C. Fernandez, X. H. Liu, J. Su, Y. X. Xie, *Meas. Control*, 51 (2018) 125.
33. S. L. Wang, C. Fernandez, M. J. Chen, L. Wang, J. Su, *J. Cleaner Prod.*, 185 (2018) 187.
34. H. Wang, S. L. Wang, E. Y. Zhang, L. X. Lu, *Sensors*, 18 (2018).
35. Y. X. Chen, D. Q. Huang, Q. Zhu, W. Q. Liu, C. Z. Liu, N. Xiong, *Energies*, 10 (2017).
36. X. W. Guo, X. Z. Xu, J. H. Geng, X. Hua, Y. Gao, Z. Liu, *Appl. Sci.-Basel*, 9 (2019).
37. D. Han, *Int. J. Aeronaut. Space Sci.*, 19 (2018) 399.
38. Y. Lei, D. D. Xia, K. Erazo, S. Nagarajaiah, *Mech. Syst. Sig. Process.*, 127 (2019) 120.
39. T. T. Liang, M. Wang, Z. H. Zhou, *Math. Probl. Eng.*, 2017 (2017).
40. R. J. Ma, H. F. Hu, S. L. Xing, Z. M. Li, *IEEE Trans. Image Process.*, 29 (2020) 3927.
41. J. L. Blanco-Claraco, F. Manas-Alvarez, J. L. Torres-Moreno, F. Rodriguez, A. Gimenez-Fernandez, *Sensors*, 19 (2019).
42. T. T. Nguyen, A. B. Khan, Y. Ko, W. Choi, *Energies*, 13 (2020).
43. H. Y. Song, J. H. Baik, *J. Ambient Intell. Hum. Comput.*, 9 (2018) 513.
44. R. Toledo-Moreo, C. Colodro-Conde, J. Toledo-Moreo, *Appl. Sci.-Basel*, 8 (2018).
45. K. Zhang, P. Zhao, C. F. Sun, Y. R. Wang, Z. W. Chen, *Chin. J. Aeronaut.*, 33 (2020) 1517.
46. C. Jiang, S. L. Wang, B. Wu, C. Fernandez, X. Xiong, *Energy.*, 219 (2020) 119603.

© 2021 The Authors. Published by ESG (www.electrochemsci.org). This article is an open access article distributed under the terms and conditions of the Creative Commons Attribution license (http://creativecommons.org/licenses/by/4.0/).